Applied Ocean Research 123 (2022) 103148

Contents lists available at ScienceDirect

Applied Ocean Research

journal homepage: www.elsevier.com/locate/apor

Evaluation of bow foils on ship delivered power in waves using model tests

J.A. Bowker, N.C. Townsend *

Faculty of Engineering and Physical Sciences, University of Southampton, UK

ARTICLE INFO

Keywords:
Ship propulsion
Waves
Bow foil
Experiment
Free running
Model tests

ABSTRACT

Bow foils have the potential to significantly reduce engine load and CO_2 emissions of ships operating in waves. This paper presents the methodology and results of an improved free running experiment for the evaluation of bow foils. The model tests directly measured the change in ship delivered power in waves with and without a bow foil. The results show that the bow foil reduces the delivered power in regular head waves by up to 50% and 12% in irregular waves. In addition to quantifying the comparative contribution due to foil thrust and reduced ship motions in waves, the experiment measured the wave phasing and feathering parameters. The presented dataset, analysis and experimental procedures, which can be used for numerical validation and performance predictions in a range of conditions, demonstrates the potential of energy saving bow foils to reduce engine load and ship emissions.

1. Introduction

1.1. Background

By harnessing the ambient wave energy, ship bow mounted foils can serve as an energy saving device (ESD), reducing the added resistance in waves and generating an additional thrust (Naito and Isshiki, 2005).

Historically, bow foils have been investigated for either propulsion in a wavy flow (Linden, 1895; Wu, 1972; Grue et al., 1988) or as anti-pitching fins on ships (Abkowitz, 1959; Stefun, 1959; Wu et al., 1996). In the 1980's research combined these topics to specifically investigate the effect on ship motions and propulsive efficiency (Jakobsen, 1981; Naito et al., 1986). Sea trials have been completed on board ships (Nikolaev M.N. and Senkin, 1995; Terao and Isshiki, 1991; Dybdahl, 1988) and bow foil technology has recently been trialled commercially (Anon, 2021c). Numerous research studies have investigated the performance of bow foils in waves, both experimentally (Bockmann and Steen, 2014; Huang et al., 2016) and numerically (Belibassakis and Filippas, 2015; Belibassakis and Politis, 2013; De Silva and Yamaguchi, 2012). Research has focused on the following main aspects; numerical prediction (Bockmann and Steen, 2016; Isshiki and Murakami, 1984), foil pitch mechanism (Bockmann and Steen, 2014; Naito and Isshiki, 2005), size and location (Feng et al., 2014; Naito and Isshiki, 2005), ship coupling (Bowker et al., 2021; Filippas, 2015; Feng et al., 2014), resistance and propulsion (Belibassakis et al., 2021; Feng et al., 2014), oblique waves (Feng et al., 2014) and free surface effects (Filippas et al., 2020).

Recently, the research focus has shifted towards investigating the effect of bow foils on ships in actual seas within the context of reducing CO_2 emissions (Belibassakis et al., 2021; Bockmann et al., 2018; Huang et al., 2016; Isshiki, 2015) and the IMO Energy Efficiency Design Index (EEDI) legislation (IMO, 2011; Feng et al., 2014; Rozhdestvensky and Htet, 2021). As indicated by the ITTC Specialist Committee on Energy Saving Methods, ESDs will require supporting evidence such as model tests for assessing propulsive efficiency and EEDI certification (ITTC, 2021a).

To date, model-scale, towed, resistance tests of a container ship and tanker with scale ratios (R) of 1:57.7 and 1:16.57, respectively, have been conducted by Feng et al. (2014) and Bockmann and Steen (2016) to evaluate the effect of fixed bow foils on ship added resistance and motions in regular waves. Both studies show similar heave motion reductions (up to 30% and 32% respectively), pitch reductions (up to 25%) and a significant reduction in ship added resistance (up to 80% (Feng et al., 2014)). Resistance tests can be used to directly assess effective power, the product of overall ship resistance and ship speed. However, as discussed in Feng et al. (2014), to estimate the delivered power (a more accurate measure of the change in engine load) requires known propulsive coefficients e.g., wake fraction, thrust deduction coefficient and propeller open water characteristics etc.

To evaluate the effect of bow foils on engine load, Bockmann (2015) and Huang et al. (2016) have conducted self-propelled model tests. In Bockmann (2015), the electrical power consumption (presented as a percentage fuel saving) of a model RoRo ship (R≈1:100) with and without a spring-loaded bow foil was measured over a range of speeds, at 3 wave periods. The results identified maximum fuel savings at full scale of 52(40)%, 84(55)% and 62(51)% in regular(irregular) head

* Corresponding author.
E-mail addresses: J.Bowker@soton.ac.uk (J.A. Bowker), nick@soton.ac.uk (N.C. Townsend).

https://doi.org/10.1016/j.apor.2022.103148
Received 15 November 2021; Received in revised form 15 March 2022; Accepted 16 March 2022
Available online 8 April 2022

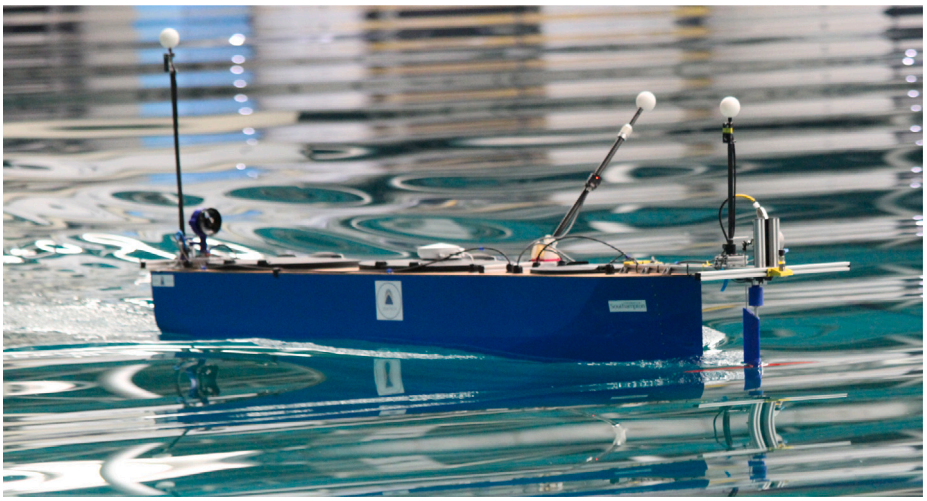

Fig. 1. Free running generic cargo ship model with bow foil.

waves over the 3 investigated wave periods (Full scale $T_p = 7,9,11$ s and $H_s = 3$ m). While Huang et al. (2016) presents experiments of a model container ship (R = 1:50), comparing the delivered power of an active pitch-oscillating bow fin to a fixed bow fin, over a range of speeds, at 2 wave periods (equal to a wavelength to ship length ratio of 1.0 and 1.3). Although no comparison with and without the foil is given, the results indicate that pitching foils may outperform fixed foils.

That is, although self propelled tests have been conducted, no direct measurement of the delivered power over a full range of wave frequencies has been performed. Furthermore, no skin friction correction (SFC) forces to account for the differences in skin friction at model scale and full scale have been applied when considering bow foils.

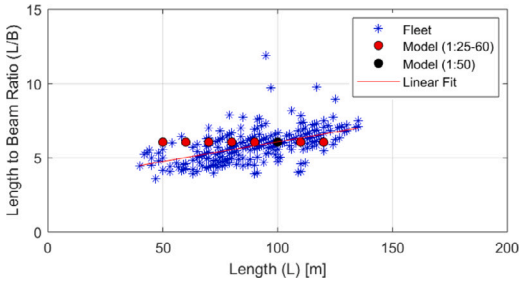

Fig. 2. Hullform particulars scatter diagram of 478 small cargo ships and various scales of the generic cargo ship design.

1.2. Paper contribution and outline

This paper provides an improved experimental methodology to evaluate the effect of bow foils on ship delivered power in regular waves and demonstrates a method to extrapolate the results to irregular waves. The results provide a new dataset on wave augmented bow foils for a generic hull form, including powering predictions, force coefficients, flapping parameters and ship motion response amplitude operators (RAO). In addition, the results identify the ratio between the reduction in added resistance in waves and the additional thrust due to bow foils.

The paper is structured as follows; Section 2 outlines the methodology including the design of the model, the experimental setup and the data handling. Section 3 details the results of the experiments in regular waves, with and without the foil, including an assessment of the ship delivered power and propulsive efficiencies in both regular and irregular waves. A discussion of the scaling considerations, relative contributions of foil thrust and added resistance and design parameters are presented in Section 4. Finally, Section 5 summarises the key insights obtained from the experimental study.

2. Methodology

2.1. Overview

To evaluate the effect of bow foils on ship delivered power, a free running model (Fig. 1) was developed and tested in regular head waves, following the ITTC torque-revolution method (QNM) (ITTC, 2021b). This approach, measuring the resultant change in propeller torque (Q) and controlled revolutions (n) to maintain a constant forward speed in waves, enabled the overall change in delivered power in regular waves, with and without a bow foil, to be experimentally measured and extrapolated to irregular waves by linear spectral analysis. To account for the relatively greater contribution of skin friction at model scale (due to the difference in Reynolds number between model and full scale) and allow direct scaling of the measured delivered power to full scale, a skin friction correction (SFC) force was applied to the model. The following section describes the design of the hullform, propulsion systems and bow foil.

2.2. Design

2.2.1. Hullform

A generic cargo ship was designed based on a collated database of 478 ships in the sub class category of small bulk carriers, according to Anon (2019). Fig. 2 shows the distribution of basis ships used in the study and highlights the range of scales that are applicable for this sub class of ships. Applying a scale ratio (R) of 1:50, the 100 m example is equivalent to 2 m in length at model scale which is a suitable size for the test facilities and equipment.

The model and equivalent full-scale hydrostatic properties are summarised in Table 1. The vertical centre of gravity (VCG) was set at 0.14 m (model scale) based on the International Code on Intact Stability (IMO, 2018), a mandatory stability criterion for cargo ships. Following the ITTC guidelines (ITTC, 2011), trip studs were implemented to promote similarity in flow regime at model scale, as summarised in Table 2.

2.2.2. Propeller and rudder

The details of the rudder and propeller design are presented in Table 2 and the general arrangement of the drivetrain is shown in Fig. 3. A 75 mm 4 bladed brass stock propeller with a P/D of 1.025 and blade

Table 1
Ship particulars.

Hull parameter	Model scale	Full scale
Scale ratio	1:50	1
Length ($L_{oa} = L_{wl} = L_{pp}$) [m]	2	100
Breath (B) [m]	0.33	16.5
Draught (T) [m]	0.12	6
Freeboard [m]	0.17	8.65
Block coefficient (C_b)	0.65	0.65
Prismatic coefficient (C_p)	0.691	0.691
Length to beam ratio (L/B)	6.06	6.06
Beam to draught ratio (B/T)	2.75	2.75
Displacement [kg, t]	51.50	6600
Volumetric displacement [m^3]	0.0515	6439
Water plane area [m^2]	0.545	1360
Wetted surface area [m^2]	0.836	2091
Vertical centre of gravity (VCG) [m]	0.14	7
Longitudinal centre of gravity (LCG), fwd of amidships [m]	0.005	0.25

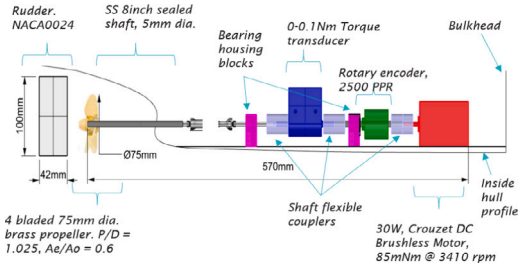

Fig. 3. General arrangement of the drive-train including the rudder and propeller.

area ratio of 0.6 was selected. The target thrust of 2.5N was based on the model scale Holtrop calm water resistance estimate at the design speed 0.8 m/s with 50% sea margin, including a thrust deduction of 0.2, a SFC correction and a 20% margin for appendage drag. The propeller selection was based on the Gawn propeller series (Gawn, 1953) with the assumption that the hull efficiency ((1-wake fraction)/(1-thrust deduction)) is equal to 1. A 24 V 30 W brushless DC motor was selected based on the max speed power of 5.3 W and a load capacity of 300% (assuming a conservative shaft efficiency of 0.5).

The rudder area was geometrical scaled following guidelines based on the ship lateral area (Liu and Hekkenberg, 2017). For simplicity, a fully balanced rudder with a NACA0024 section was selected providing reasonable thickness for a rudder stock at 25% of the chord length (measured from the leading edge). The rudder was 3D printed in PLA (100% infill). The hull, rudder and propeller clearances followed the recommendations in Molland et al. (2017).

2.2.3. Bow foil

A neutrally buoyant, rectangular, bow foil with a (uniform) NACA0012 section was 3D printed in PLA, as summarised in Table 2 and shown in Fig. 4. The foil was mounted at 10% of the model length forward of the bow, which ensured that the foil operated in the free undisturbed flow stream.

Following studies that flapping bow foils may outperform fixed foils (Huang et al., 2016), and as a precursor to active control strategies which remains challenging (see Huang et al. (2016), Bockmann and Steen (2014)), a passive, spring-loaded foil was selected for this study. The foil setup is shown in Fig. 4. A numerical model based on previous work (Bowker et al., 2021) was used to derive the spring constant (0.165 Nm/rad) and foil size (aspect ratio, AR = 7).

The spring loaded foil was free to pitch up to +/- 45 degrees, pivoting at 10% of the chord length (from the leading edge), and measured using an encoder linked to a parallel pitching rod. Torque springs, located at the top and bottom of the pitching rod, were used to ensure a symmetric spring load.

Table 2
Model rudder, propeller, bow foil and trip stud detailed information.

Property	Value	Comment/Rationale
Rudder area [mm^2]	4200	Typ. $Area/(L \times T) \geq 1.7$
Rudder span [mm]	100	2.5 mm from keel
Rudder chord [mm]	42	Aligned with transom
Propeller blades	4	
Propeller diameter [mm]	75	
Propeller P/D ratio	1.025	
Propeller A_e/A_o ratio	0.6	
Propeller tip clearance [mm]	20.25	Typ. $\leq 25\%$ D
Propeller rudder spacing [mm]	24	Typ. 0.3 to 0.35 D
Foil section	NACA0012	
Foil chord, c [mm]	60	
Foil span, s [mm]	420	
Foil aspect ratio	7	
Foil mass [$grams$]	329	incl. vertical strut
Foil pivot point, x_p [mm]	6	10% chord from the L.E.
Foil lever arm pivot point [mm]	33.75	from the L.E.
Foil longitudinal location [mm]	1200	from the LCG
Foil depth [mm]	120	located at the keel line
Stud height [mm]	2.5	Reynolds roughness criteria
Stud diameter [mm]	3.2	Similar models
Stud spacing [mm]	25	ITTC guidelines
Stud location [mm]	100	Typ. $5\%L$

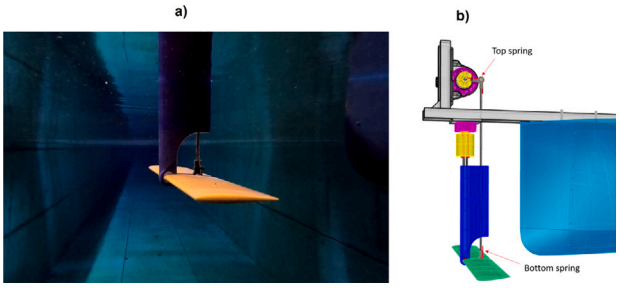

Fig. 4. Neutrally buoyant, spring loaded foil mounted to the bow of the model (a) Underwater image (b) CAD rendering.

The entire bow foil component was secured to a protruding aluminium structure at the bow via a tri-axial load cell, as shown in Fig. 1. The tri-axial load cell was calibrated in compression and tension for the vertical (Z) force, including a compensation for the sensor's self weight. The horizontal forces (X,Y) were calibrated at the foil pivot location, in addition to directly at the load cell confirming that the induced moments had a negligible effect on the measured forces.

2.2.4. Skin friction correction

For a towed model, a weight is usually connected via a pulley to apply the SFC force (Seo et al., 2020) but for a free running model the additional thrust force is often applied using an air fan (Ueno and Tsukada, 2016). In this study, a ducted air fan was mounted to the stern, as shown in Fig. 1. This was attached to a load cell in order to calibrate and set the fan input control to the forward thrust. The required SFC load was calculated from the difference between the model and full-scale skin friction coefficient (i.e. $\Delta C_f = Cf_m - Cf_s$) using the ITTC '57 frictional correlation line based on the respective Reynolds Number for the model and ship speeds (ITTC, 1957).

The calculation of the SFC force was completed for the Reynolds number of the full scale ship of 100 m with a design speed of 11 knots and was calculated to be 0.72N. For a range of Reynolds numbers from 0.3×10^9 to 1.2×10^9, the SFC forces vary from 0.70N to 0.75N, respectively. This range is equivalent to a full scale ship length range of 75 m to 175 m, assuming constant Froude scaling. Therefore, assuming

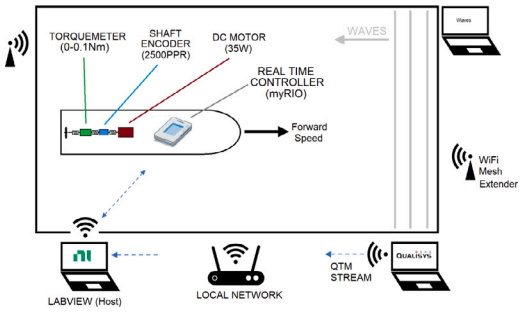

Fig. 5. Schematic outlining the experimental setup and realtime control.

Table 3
Sensor information.

Sensor	Type	Range
Wave probe (at bow foil)	Ultrasonic	50–200 mm
Facility wave probes	Ultrasonic	50–2500 mm
Tri-axial load cell	Half bridge	±10 N
Foil pitch encoder	Optical	2048 ppr
Motion capture (Qualisys)	Optical	–
Accelerometer	Tri-axial	±8 g
Shaft torquemeter	Full bridge	0–0.1 Nm
Shaft encoder	Optical	2500 ppr
SFC load cell	Full bridge	±5 N
Rudder potentiometer	Resistance	±50 deg

a linear response the non-dimensional results presented in this paper are applicable to a range of bulk carriers including both 'Small' and 'Handysize' classes (Anon, 2019), with less than 1% error due to the variation in SFC.

2.3. Experimental setup

2.3.1. Data acquisition and control

Fig. 5 outlines the experimental setup for the data acquisition (DAQ) and control. The onboard data acquisition and control system (located in the central watertight compartment of the model) was based on a National Instruments myRIO1900 and Labview software, following a robotic architecture of plan-sense-act. A local wireless network was setup to view and control the real time Labview VI (model) from a laptop (host) remotely.

The ship motions were tracked about the longitudinal centre of gravity (LCG) in real time using a Qualisys motion capture system and recorded on a local computer. To control the forward speed, the motions were streamed to the model (via a host VI) and a proportional–integral (PI) feedback controller used to maintain the forward speed through propeller rpm changes. The rudder angle was controlled by a radio-controlled servomotor and measured by a potentiometer attached to the rudder stock housed in the transom.

The shaft torque and revolutions per minute (RPM) were measured onboard with a torquemeter and rotary encoder, respectively. A tri-axial load cell was used to measure the foil loads and an incremental encoder was used to measure the foil pitch. In addition, an ultrasonic wave probe was used to measure the incident wave profile. A list of sensors is presented in Table 3.

All the data was recorded at a sample rate of 100 Hz. The waves were recorded using 9 different wave probes situated around the test facility.

2.3.2. Test matrix and method

Regular waves were selected to capture the peak frequencies of the equivalent full scale (Ls = 100 m) ITTC sea state of H_s = 2 m and T = 7s, as shown in Fig. 6. All tests were completed with and without the bow foil including calm water runs at 0.8 m/s (11 knots full scale

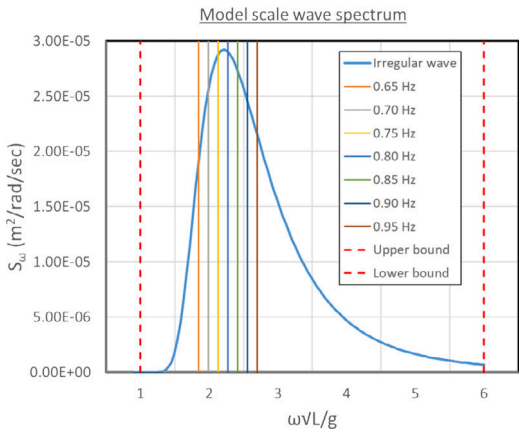

Fig. 6. Regular wave frequencies derived from full scale irregular wave spectrum (ITTC, H_s = 2 m, T = 7s).

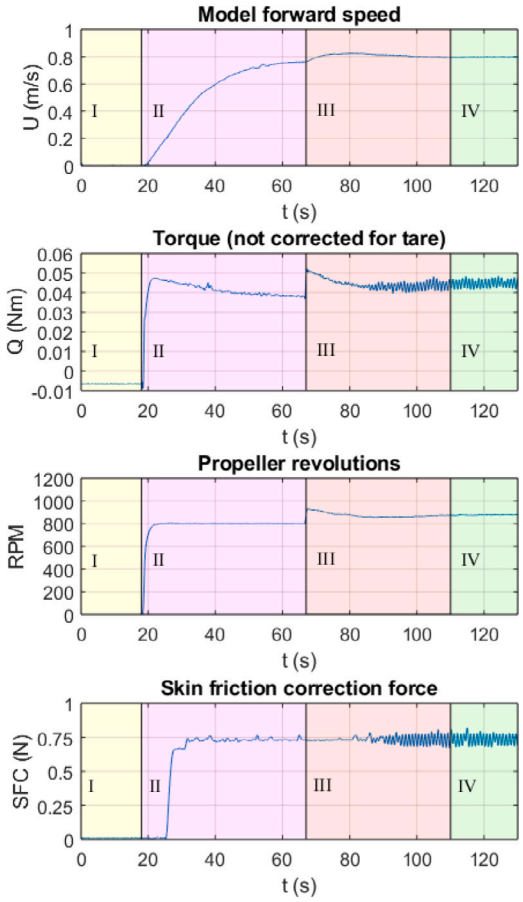

Fig. 7. Example time history of propulsion data (I: Datum, II: Acceleration under fixed RPM control, III: Transient stage with switch to autopilot and ramping of waves, IV: Steady state stage for at least 10 wave encounters).

equivalent) to measure the baseline delivered power. Measurements of the ship motions and foil response were also recorded using the onboard data acquisition system.

The experiments were conducted at the QinetiQ ocean basin (Length = 120 m, Breadth = 60 m, Depth = 5 m). Table 4 outlines the conditions for the series of tests. The temperature of the water was recorded to calculate the SFC force and the wave amplitude was set based on the ITTC guidelines for testing in regular waves (ITTC, 2017a), which recommends a wave height to wavelength ratio of 1/50.

Table 4
Experimental Investigations.

Parameter	Value
Wave amplitude $[m]$	0.02
Wave frequencies $[Hz]$	0.65, 0.7[a], 0.75, 0.8[a], 0.85, 0.9, 0.95
λ/L	1.85, 1.59, 1.39, 1.22, 1.08, 0.96, 0.86
Ship heading $[deg]$	180 (head waves)
Ship model speed $[m/s]$	0.8
Froude number $(V/\sqrt{gL})$	0.18
SFC force $[N]$	0.72 @ 15.5 ^{o}C

[a]Repeat runs.

Table 5
Model condition values.

Parameter	Measured
Mass [kg]	51.75
Pitch radius of gyration, k_{55} [m]	≈25% L
Vertical centre of gravity, KG [m]	0.1334
Metacentric height, GMt [m]	0.0136
Roll period [s]	2.336
Bow foil spring constant [Nm/rad]	0.165

The experimental procedure (illustrated in Figs. 7 and 8, as an example) comprised of a zero speed datum (I), followed by an initial acceleration in calm water over ≈40 m under fixed rpm control (II), before switching to autopilot control, encountering waves (III) and settling into a steady state response (IV) (with a controlled average model speed of 0.8 m/s and at least 10 wave encounters recorded). To reduce any uncertainty from residual wave energy, the time between runs was set to at least 15 min and residuals were kept to less than 5%. In addition, calibrations and shaft residual torque (tare) measurements were conducted before and after the experiment to check for any drift.

The model was conditioned prior to the experiments and the resultant values are presented in Table 5. An inclining test was conducted to measure the vertical centre of gravity and a compound pendulum rig was used to measure the radius of gyration. The natural roll period was determined from repeat roll decay tests. The model was ballasted to 0.12 m draft and set to zero trim and heel.

2.4. Data handling

2.4.1. Post processing

The data was processed using the following steps:

- *Synchronise:* all data formats were synchronised to the same time base. The DAQ accelerometer was used to synchronise the data recorded onboard with the ship motions data recorded locally.
- *Crop:* the data was cropped into a datum at the start of the run (Fig. 7-I) and a steady state response comprising of at least 10 wave encounters (Fig. 7-IV).
- *Filter:* the data was filtered using a Butterworth low-pass filter with a cutoff of 10 Hz for the rudder and foil encoder, 5 Hz for the motions and foil forces, 2 Hz for the torquemeter and 1 Hz for the SFC fan load and the RPM encoder.
- *Analyse:* the harmonic results were analysed using sine wave fitting to identify the amplitude, phase and encounter frequency.
- *non-dimensionalise:* the results were non-dimensionalised with respect to both the frequency and magnitudes of response.

2.4.2. Uncertainty

The overall uncertainty was assessed following the ITTC recommended procedures (ITTC, 2017a), as a combination of Type A ($u(A)$) and Type B ($u(B)$) uncertainty. Type A referring to the uncertainty due to the statistical variation of repeated measurements and experimental parameters, and Type B the uncertainty associated to experimental measurement. To assess the repeatability (ITTC Type A uncertainty), 3 repeats at 2 wave frequencies were conducted. Although the number of repeats is low, compared to the ITTC guidelines for Type A uncertainty analysis, the assessment provides a useful indication of the experimental repeatability and, in accordance with the ITTC recommendations for a small number of repeats (< 10) (ITTC, 2008), an inverse Student t correction at the 95% confidence level ($t_{95} = 2.92$) has been included in Table 8.

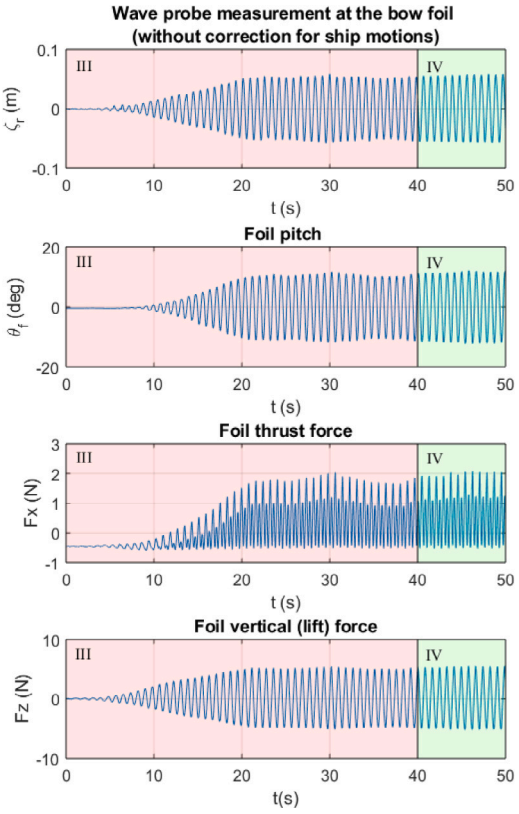

Fig. 8. Example time history of foil data (III: Transient stage, IV: Steady state stage).

Table 6
Overall standard deviation of the experimental parameters from all 22 runs in waves (% values are calculated as the difference relative to the target value).

Parameter	Standard deviation
Wave amplitude	3.81%
Speed	1.02%
SFC	2.22%
Heading	0.57 deg
Rudder	4.25 deg

The Type A uncertainty, based on three repeats at two frequencies (0.7 and 0.8 Hz) and presented in Table 6, were found to be < 5%. For Type B, the torquemeter and loads cells were calibrated according to the National Physics Laboratory (NPL) guidelines (Robinson, 2008). The torquemeter calibration results, Table 7, show that measurement tolerances of ± 1 mNm were achieved. With the shaft RPM measured by a digital encoder with 2500 pulses per revolution, the Type B uncertainty of the delivered power measurement was calculated to be less than 5%.

The resultant standard uncertainties, considered acceptable for full scale prediction, are included in the figures as error bars and summarised in Table 8.

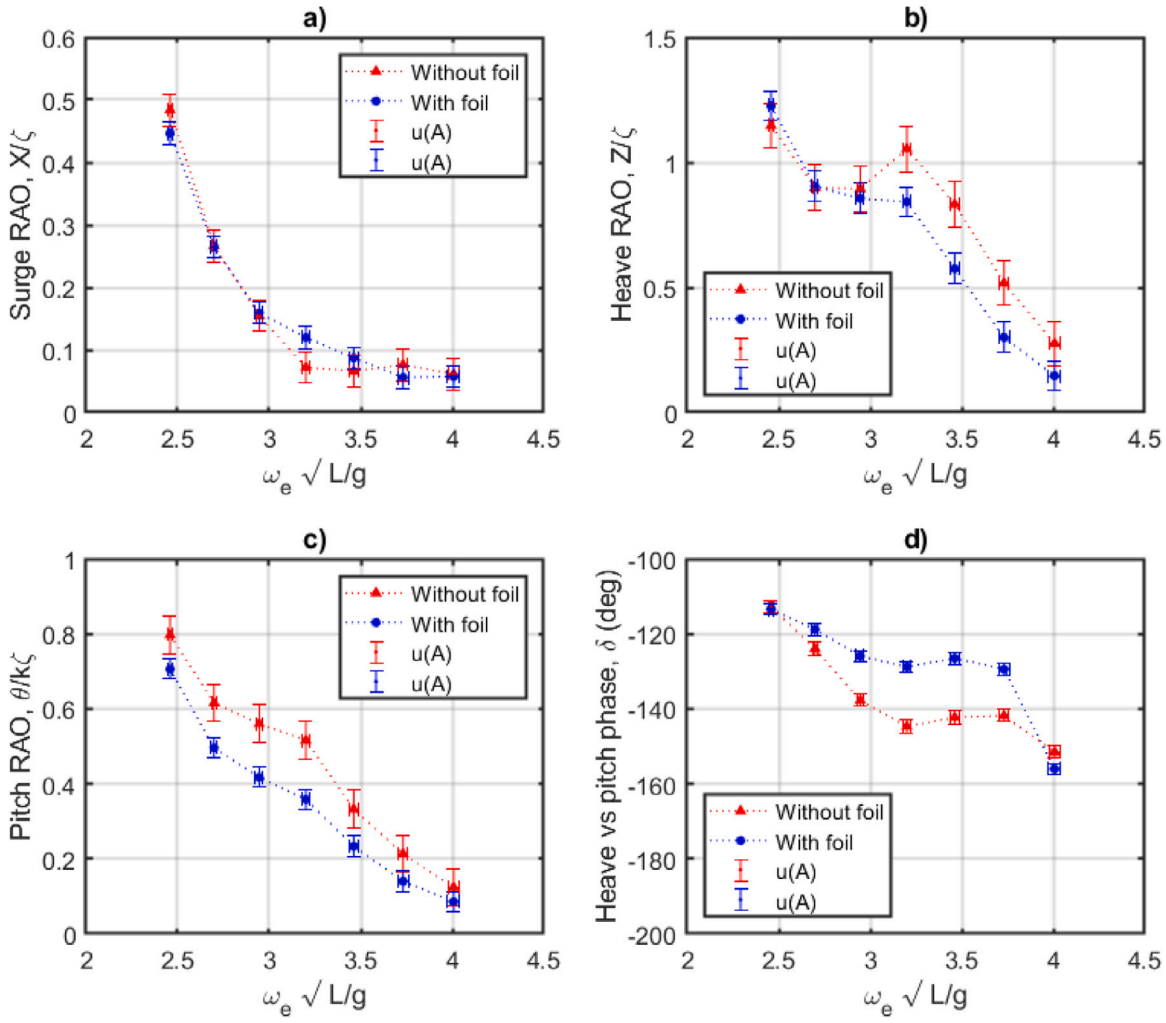

Fig. 9. Motion RAOs and phase; (a) Surge, (b) Heave, (c) Pitch and (d) Phase.

Table 7
Torquemeter calibration and Type B uncertainty.

Parameter	Value
Overall uncertainty	4.32%
Linear fit (R^2)	0.99971
Reproducibility*	3.7%
Repeatability (overall)	1.62%, 1.03%
Repeatability (F.S)	1.97%, 1.37%
Departure from fit	−0.646, −0.391%
Departure from fit (F.S)	−0.78, −0.489%
Hysteresis	1.3%, 0.84%
Hysteresis (F.S)	1.799%, 1.921%
Creep (Overall)	−0.18%
Creep (recovery)	−0.07%

3. Results

3.1. Ship motions

Fig. 9 shows the surge, heave and pitch response amplitude operators (RAOs) with and without the bow-foil. The results were nondimensionalised using the measured wave amplitude and wave slope, in the case of the pitch RAO. The results clearly show that the presence of the bow-foil acts to reduce the pitch and heave motion of the vessel in head seas, with minimal effect on the surge motion. An average reduction of approximately 10% and 20% in heave and pitch, respectively, was measured. The greatest reduction was observed at the wave frequency of 0.8 Hz, which equates to a wavelength to ship length (λ/L) of approximately 1.2. Fig. 9(d) shows the phase difference between vessel heave and pitch with and without the foil. This result shows that the foil has a significant effect on the phase response of the vessel motion and is most pronounced around a λ/L of 1.2.

3.2. Foil forces

The vertical force (Fz) and the horizontal thrust force (Fx) measurements, presented in Fig. 10, have been nondimensionalised with respect to wave amplitude. The full scale equivalent forces for a 100 m ship equate to a maximum amplitude of ~ 750 kN in Fz and a maximum of ~ 375 kN in Fx.

The horizontal thrust force (Fx) has two peaks within one heave oscillation, due to the generation of thrust in both the upstroke and downstroke. Interestingly, the thrust amplitude during the upstroke is greater than the downstroke, as shown in Fig. 10. This finding is likely to be due to a contribution of both the phase response relative to the oscillating flow of the incident wave profile and the increase in drag on the vertical strut when it is submerged during the downstroke.

3.3. Delivered power

The delivered power was measured directly over the range of regular waves and then extrapolated to an irregular wave sea state using linear spectral analysis.

Table 8
Standard uncertainty values for the seakeeping tests with and without the bow foil, including the Student's t corrected values for a 95% confidence level in brackets.

Measurement	ITTC type	With foil	Without foil
Surge $[X/\zeta]$	A	0.0175 (0.0511)	0.0252 (0.0736)
Heave $[Z/\zeta]$	A	0.0604 (0.1764)	0.0902 (0.2634)
Pitch $[\theta/k\zeta]$	A	0.0270 (0.0788)	0.0498 (0.1454)
Phase diff. $[deg]$	A	1.5358 (4.4845)	1.6392 (4.7864)
Foil thrust force $[N]$	A	0.0374 (0.1091)	–
Foil vertical force $[N]$	A	0.2425 (0.7082)	–
Foil pitch $[deg]$	A	0.6578 (1.9209)	–
Delivered power $[W]$	A & B	0.2178 (0.3826)	0.2752 (0.5882)

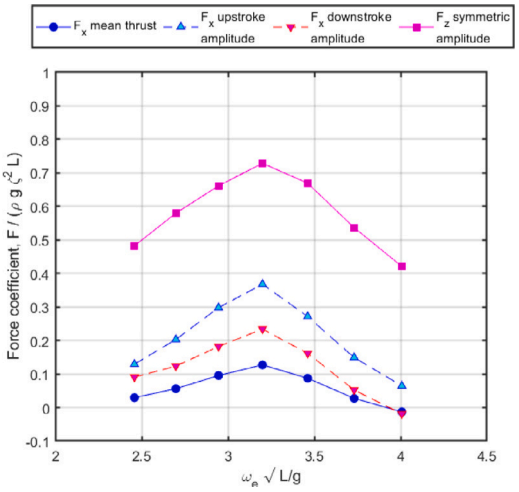

Fig. 10. Non dimensional mean and amplitude vertical (Fz) and horizontal forces (Fx) acting on the flapping foil and vertical strut.

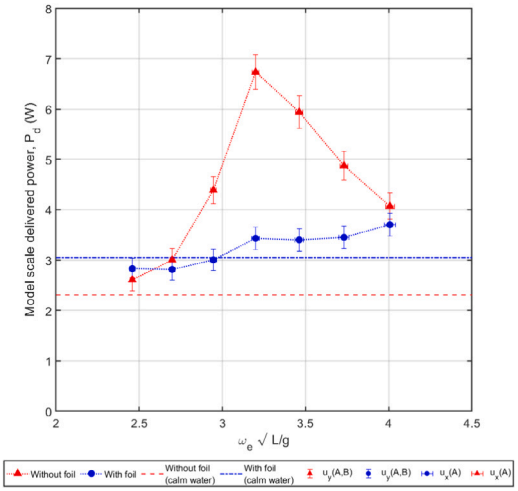

Fig. 11. Model scale delivered power results in calm water and waves for with and without the bow foil.

3.3.1. Regular waves

Fig. 11 shows the model scale delivered power with and without the bow-foil in regular head waves and calm water. The model scale delivered power (P_d) was calculated from the measured shaft revolutions per second (n) and the measured shaft torque (Q) with a correction for the shaft tare (Q', bare torque without propeller). That is;

$$P_d = 2\pi n(Q - Q') \tag{1}$$

The percentage reduction in total delivered power due to the action of the bow foils is presented in Fig. 12. The percentage reduction ranges from 30 to 50% between the wavelength to length ratios of 1 and 1.4, respectively, with a peak at approximately 1.2. This represents a significant energy saving in head seas with the use of the bow foil, which is also shown to be effective over a wide range of wave frequencies.

In calm water the additional drag of the foil and strut equated to a 32% increase in model scale delivered power, indicating that a retractable foil system would most likely be required in practise.

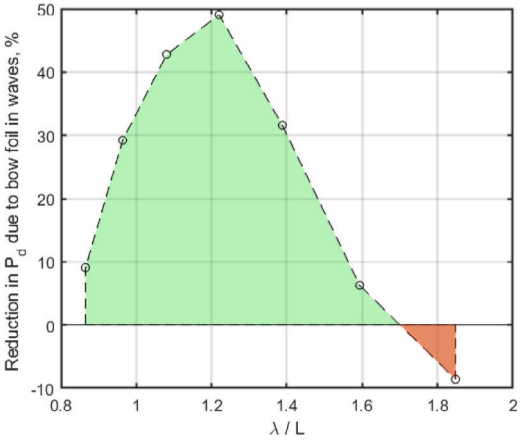

Fig. 12. Percentage reduction in delivered power with a bow foil in waves.

3.3.2. Irregular waves

The percentage reduction in delivered power in irregular and oblique waves was predicted based on the results in regular waves by applying linear spectral analysis. This method assumes that the change in propeller torque and revolutions in waves is proportional to the square of the wave amplitude. From this assumption, the change in torque ($\delta Q(\omega)$) and propeller revolutions ($\delta n(\omega)$) were analysed with respect to the wave frequency as a transfer function to evaluate the spectral response ($\delta Q_{b,f}, \delta n_{b,f}$) relative to a directional irregular wave spectrum.

The change in torque and propeller revolutions were evaluated at each wave frequency relative to the calm water results without the bow foil (Q_{sw}, n_{sw}, P_{sw}), then integrated over the range of wave frequencies (ω) and relative headings (α):

$$\delta Q_{b,f} = 2\int_0^{2\pi}\int_0^{\inf} \frac{\delta Q(\omega)_{b,f}}{\zeta^2} E(\omega,\alpha,H,T,\phi)d\omega d\alpha \tag{2}$$

$$\delta n_{b,f} = 2\int_0^{2\pi}\int_0^{\inf} \frac{\delta n(\omega)_{b,f}}{\zeta^2} E(\omega,\alpha,H,T,\phi)d\omega d\alpha \tag{3}$$

The subscript b refers to the ship with a bare hull, i.e. without a foil, and f refers to the ship with a bow foil installed. To account for oblique waves, a cosine squared spreading function (for head seas) was assumed to be a reasonable approximation based on the turning circle response in waves (as shown in Fig. 13). The torque and propeller revolutions are combined to calculate the overall change in delivered power in the

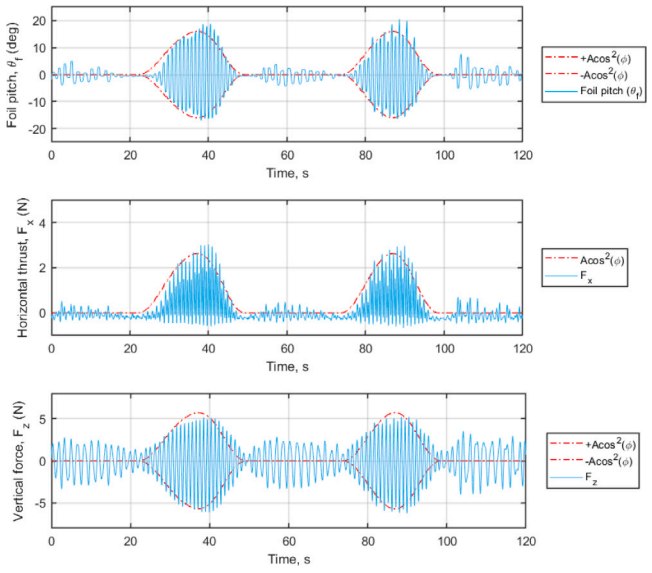

Fig. 13. Time history results for foil pitch and forces during a turning circle in 0.8 Hz regular waves at a speed of 0.8 m/s, with cosine squared ($90° < \phi < 270°$) heading relationship superimposed.

irregular wave ($\delta P_{b,f}$) which was then used to estimate the percentage reduction in delivered power in waves (η_w):

$$\delta P_{b,f} = 2\pi[(Q_{sw} + \delta Q_{b,f})(n_{sw} + \delta n_{b,f}) - Q_{sw} n_{sw}] \tag{4}$$

$$\eta_w = \frac{\delta P_b - \delta P_f}{P_{sw} + \delta P_b}\% \tag{5}$$

The aforementioned calculations were performed for the case study ITTC sea state of 2 m significant height and 7s period and setting the wave frequency limits to the extents of the spectra (i.e lower at $\omega\sqrt{L/g} = 1$, upper at $\omega\sqrt{L/g} = 6$), as shown in Fig. 6. At these frequency limits for the bow foil calculation, the change in torque and revolutions is assumed to converge to the difference between the calm water values for with and without the bow foil. While without the foil, the change in torque and revolutions converges to zero i.e. calm water.

In an irregular sea state with no directional spreading, the increase in delivered power was 51% without the foil compared to 29% with a bow foil. Assuming that the bow foil is retracted in following seas, the increase in delivered power in an irregular sea state including directional spreading was 39% without the foil compared to 22% with the bow foil. That is, the bow foil is estimated to provide a 12% reduction in delivered power as calculated using Eq. (5).

4. Discussion

4.1. Ship propulsion

The experimental results show a significant reduction in delivered power in regular head waves, with the greatest reductions (up to 50%) at $\lambda/L \approx 1.2$. The principal of operation of the foil mechanism was found to be twofold:

- The foil generates a net thrust force, reducing the delivered power required to maintain a given speed in waves, and
- The foil reduces the pitch and heave motion of the vessel, reducing the added resistance in waves

The design of the foil will affect the ratio of these two mechanisms and it is, therefore, important to understand the contribution to the overall change in delivered power. Using the measured foil thrust,

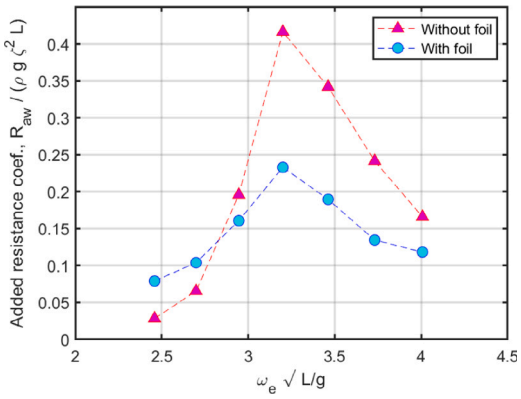

Fig. 14. Extrapolated added resistance from the experimental dataset for with and without the foil.

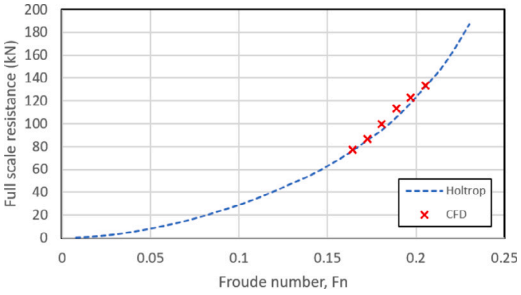

Fig. 15. Total barehull resistance curve using Holtrop regression method and computational fluid dynamics (CFD) for the 100 m full scale ship.

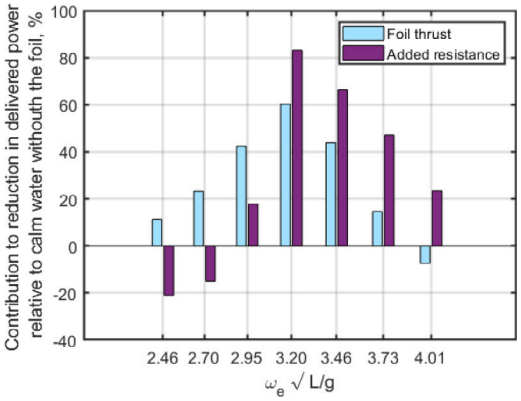

Fig. 16. Percentage contribution to the reduction in delivered power due to foil divided into foil thrust and reduction in added resistance.

assuming a hull efficiency of unity and small deviations in propulsive coefficient (QPC) in waves, the estimated percentage contributions due to foil thrust and reduction in added resistance (normalised relative to the calm water effective power) were calculated and are shown in Figs. 14 and 16. The effective power was evaluated using the Holtrop method for the design speed at model scale. The Holtrop regression method was verified using computational fluid dynamics simulations at full scale, presented in Fig. 15. The estimated model scale effective power was then divided by the measured calm water delivered power without the bow foil to estimate a QPC value of 0.59. However, this is not an exact method and has only been used to provide an estimate of the relative effect of a change in added resistance compared to the additional thrust provided by the bow foil.

The estimated added resistance in waves with the bow foil installed is approximately half of that without the bow foil. The assumption of

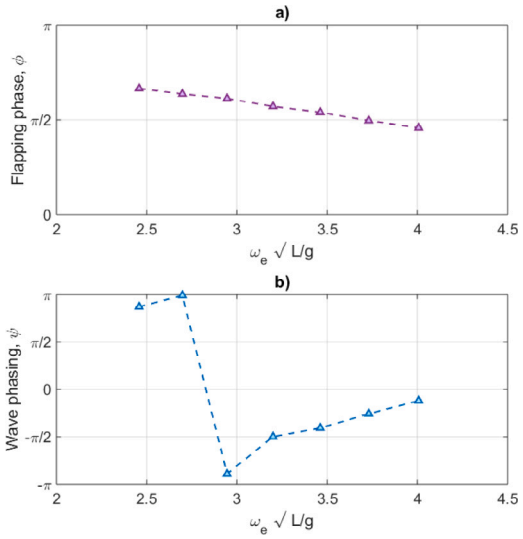

Fig. 17. (a) Flapping phase difference between induced foil heave and pitch, (b) Wave phasing parameter (the value for the median wave frequency did not measure due to exceeding the wave probe limits and is therefore plotted as an interpolated value).

constant QPC is based on a constant propeller advance coefficient (J), which is only strictly valid for the case with the bow foil. Without the bow foil, the large load variation in waves results in $\pm 5\% J$, which equates to a similar variation in QPC and uncertainty in the added resistance estimations.

With the bow foil, it can be seen in Fig. 16 that the reduction in added resistance in waves is greater than that of the foil thrust for higher wave frequencies. This is reflected in Fig. 14 whereby the added resistance in waves is larger at higher wave frequencies and noticeably less for wavelengths close to twice the length of the ship. The phase change at wavelengths greater than 1.5 times the ship length ($\omega_e \sqrt{L/g} < 2.8$) shows a negative effect of the foils on the added resistance in waves, which could be attributable to a phase change in the heave response of the ship, as shown in Fig. 9. The contribution of foil thrust is shown to be effective over the full range of wave frequencies, except for the highest wave frequency (short wavelength, $\lambda/L = 0.86$) which is associated with the phase difference between the foil motions and the wave orbital velocities.

4.2. Flapping and wave phasing

The flapping phase is the phase difference between the foil heave and pitch motion. If the flapping phase is less than $\pi/2$ the foil pitch is positive at the point of maximum heave, and negative for phase values greater than $\pi/2$. The results shown in Fig. 17(a), show that the foil mostly responds at flapping phases greater than $\pi/2$ which represents a small lag in the passively sprung pitch response whereby maximum pitch occurs slightly after the maximum foil heave velocity. This phase response is likely to result in larger vertical forces and less propulsive efficiency, as indicated by De Silva and Yamaguchi (2012). This is potentially a parameter, along with foil feathering (discussed in the next section), that can be used to control foil thrust and ship motions.

The wave phasing is defined as the phase difference between the foil heave motion and the wave orbital velocities, such that $-\pi/2$ equates to the foil heave velocity and wave velocity being out of phase (De Silva and Yamaguchi, 2012). When these parameters are out of phase, maximum energy is extracted from the incident wave due to a superposition of the flow over the flapping foil.

This experiment determined the wave phasing parameter by measuring the incident wave profile using a ultrasonic wave probe mounted directly above the foil. The motions of the ship were mapped to the foil location and the wave probe data was corrected for induced ship motions relative to the waves. This method also allowed for the measurement of the ship induced foil heave. From this dataset, it was possible to calculate the wave phasing parameter, shown in Fig. 17(b).

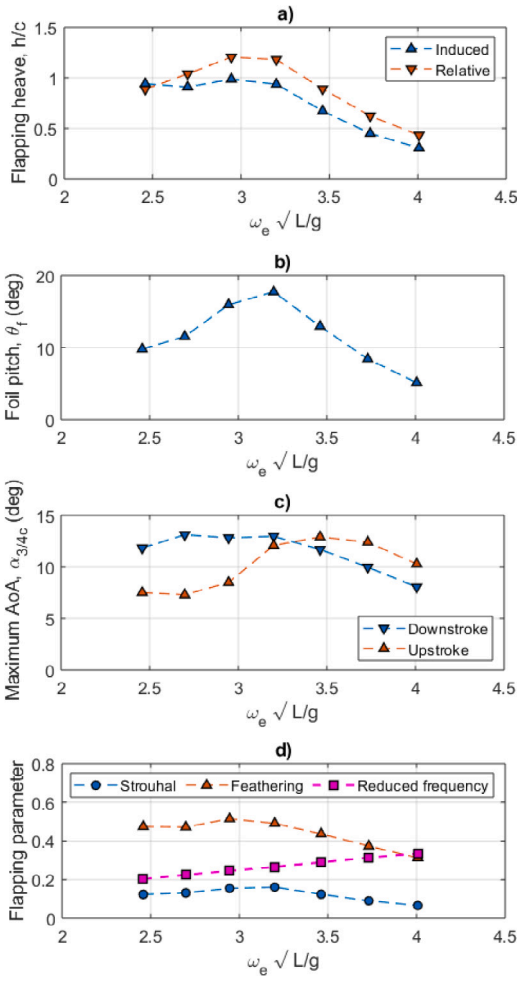

Fig. 18. (a) Flapping induced and relative foil heave amplitude; (b) Spring loaded foil pitch amplitude; (c) Effective angle of attack at the 3/4 chord location; (d) Strouhal and feathering numbers, and Reduced frequency.

The results show that the optimal wave phasing of $-\pi/2$ (± 0.5 rad) occurs at wavelength to ship length ratios of approximately 1.05 to 1.25, which is also the range of maximum foil thrust and change in delivered power shown in Figs. 11 and 16, respectively. This is in agreement with the numerical results published by Bowker (2018) and De Silva and Yamaguchi (2012), Filippas and Belibassakis (2014) and, to the authors knowledge, is the first experimental confirmation of the wave phasing parameter.

4.3. Flapping characteristics

The non-dimensional foil heave amplitude is presented in Fig. 18(a), and shows the decrease in amplitude with wave frequency. The induced heave (h_i) is the heave purely from the ship motions, whilst the relative heave (h_r) accounts for the wave orbital motions at the depth of the foil. For all wave frequencies, the relative heave is larger than the induced heave which highlights the importance of the wave phasing parameter. At the limits of the wave frequency the effect is minimised and there is clearly an optimum wavelength to ship length ratio for extracting maximum energy from the incident waves.

The foil pitch response (θ_f) is presented in Fig. 18(b) as the amplitude of the sinusoidal pitch motion. The neutrally buoyant, sprung loaded foils, oscillated about zero degrees (in-line with the keel-line) and the largest pitch response was found to align with the maximum reduction in delivered power.

Through combination of the foil heave and pitch, the ship speed (U) and pitch (θ), and the instantaneous wavy flow, it was possible to estimate the effective angle of attack at the three-quarter chord location ($\alpha_{3/4c}$), as proposed by Pistolesi (1933):

$$\alpha_{3/4c} = \tan^{-1}\left(\frac{V_w - \dot{h} - (3/4 - x_p)c\dot{\theta}_f}{U - U_w}\right) - \theta_f - \theta \tag{6}$$

where x_p is the pivot point as a fraction of the chord from the leading edge, and U_w and V_w are the instantaneous horizontal and vertical wave orbital velocities, respectively, which were estimated from the wave probe measurements and corrected for the depth of the foil. The maximum effective angle of attack, Fig. 18(c), is estimated to be less than 15 degrees and shows an asymmetry between the upstroke and downstroke.

In the case of bow foils, the feathering parameter is calculated as the ratio of foil pitch and heave, and the ratio of ship speed and wave encounter frequency (ω_e), with consideration for the relative foil heave at the foil mean depth (d) (De Silva and Yamaguchi, 2012):

$$\epsilon = \frac{\theta U}{\omega_e(h + \frac{g\zeta k}{\omega\omega_e}e^{-kd})} \tag{7}$$

The feathering parameter, shown in Fig. 18(d), can therefore be optimised through careful design of the foil pitch response. The results show that the feathering parameter ranges from 0.35 to 0.55, which is close to the region of maximum propulsive efficiency (0.7) according to De Silva and Yamaguchi (2012). This is an important outcome for the design of future bow foil systems that use either actively or passively pitching foils. Similar to flapping phase, the feathering parameter will also have an effect on the ratio between the resultant vertical and horizontal forces and should therefore be considered as a parameter to control the foil thrust and the reduction of ship motions.

The Strouhal number ($St = 2fh/U$, where f is flapping frequency, h is heave amplitude and U is ship speed) has been shown to be an important metric for the propulsive efficiency of flapping foil propulsion with optimum values of between 0.25 and 0.35 (Triantafyllou and Gopalkrishnan, 1991). The tests measured a mean Strouhal number of 0.13, as shown in Fig. 18(d). Whilst this is an interesting observation, the parameters that govern the Strouhal number for bow foil wave propulsion are dictated by the ship speed, scale and environment, all of which are predetermined. In addition, the reduced frequency ($k_f = \omega_e c/2U$) is an important metric in the analysis of flapping foil dynamics and was measured to be between 0.2 and 0.35, as shown in Fig. 18(d).

4.4. Additional considerations

4.4.1. Model scale

The model scale presents a scaling conflict between the ship motions and the drag (hull) and lifting surfaces (bow foil, propeller and rudder) since the former is governed by Froude number and the latter by Reynolds number. Froude scaling has been implemented due to the dominance of gravity waves on the overall seakeeping response. However, to achieve flow regimes similar to full scale the model would need to be an order of magnitude larger, which is not practical for tank testing. Therefore, the difference in Reynolds number for the hull resistance was mitigated using a skin friction correction force and trip studs. The skin friction correction force acts to compensate for the additional hull drag force at the lower Reynolds number (model scale) and, therefore, enables the scaling of propeller loading for the purposes of assessing the change in delivered power in waves. This method does not, however, compensate for the change in inflow velocities at the propeller due to Reynolds number which is considered beyond the scope for this comparative seakeeping assessment. The required SFC load was calculated using the ITTC '57 frictional correlation line but an improved approach, accounting for the form factor and roughness correction, could be achieved using the ITTC '78 procedure (ITTC, 2017b).

4.4.2. Foil scale

A comparison between the measured lift force coefficient and the theoretical prediction using Theodorsen's linearised unsteady foil theory (Theodoersen, 1935), which assumes fully attached flow, is presented in Fig. 19. The predicted lift force (L) was evaluated using the measured foil motions (heave and pitch) and the estimated angle of attack including the modified lift deficiency factor for finite span ($\frac{AR}{AR+2}C(k_f)$) (Jones, 1940), calculated from the aspect ratio (AR) and reduced frequency (k_f):

$$L = \frac{AR}{AR+2}C(k_f)\alpha_{3/4c}\pi\rho V^2 cs + m_a(-\ddot{h}_r - (1/2 - x_p)c\ddot{\theta}_f - U\theta_f) \tag{8}$$

where V is the effective flow speed, estimated at the three-quarter chord location ($V = \sqrt{((V_w - \dot{h} - (3/4 - x_p)c\dot{\theta}_f)^2 + (U - U_w)^2)}$), and m_a is the added mass of a flat plate ($m_a = \rho\frac{\pi}{4}c^2 s$).

The results, in Fig. 19, show good agreement between the measured and predicted lift forces, providing confidence in the linearisation of the bow foil lift force for full scale prediction. Although, the estimated experimental angles of attack exceed the model scale stall angle, the results do not exhibit non-linearities in the measured lift force. This finding, in agreement with Ol et al. (2009), suggests that the existence of any flow separation does not significantly affect the resultant lift force, at this scale (i.e. Reynolds Number). This could be attributed to the effects of a dynamic angle of attack which acts to delay stall, discussed in detail by Bockmann (2015).

The Reynolds number for the foil is 4.2×10^4 at model scale and 15×10^6 at full scale, which results in laminar and fully turbulent flow regimes, respectively. This difference in the flow regimes significantly increases the stall angle (the angle beyond which flow separation is expected to occur) for a NACA0012 foil from 8° at model scale (Miley, 1982) to 16° for full scale (Abbott and Von Doenhoff, 1959). Therefore, provided the foil pitch response is the same at full scale the estimated angles of attack are also equivalent, which effectively reduces the likelihood of dynamic stall at full scale (compared to model scale), providing further confidence in the foil scaling.

In addition, the absence of stall suggests that flow separation is minimised which reduces the Reynolds number dependence on both lift and drag. Therefore, assuming kinematic similarity and Reynolds number independence, the foil forces can be non-dimensionalised by wave amplitude (presented in Fig. 10). For larger angles of attack, a Reynolds number correction can be applied for scaling, as demonstrated by Bockmann and Steen (2016).

4.4.3. Practicality

In practice a retractable foil system would most likely be required, for example in calm water to avoid the additional appendage drag, in large seas for safety and potentially when moored/in port to avoid thrust and for safety. With various retraction mechanisms and fixed, passive and active foil types, assessing the operational loads and performance in real seas of bow foils remains a challenge and further research is needed. While this paper presented the model scale loads from a sprung loaded foil in regular waves, when considering the full-scale loads the authors would recommend a safety factor is added. Furthermore, caution in extrapolating the results for fixed foil arrangements is advised as the loads are expected to be greater due to the larger angles of attack experienced by a purely-heaving foil (Ol et al., 2009).

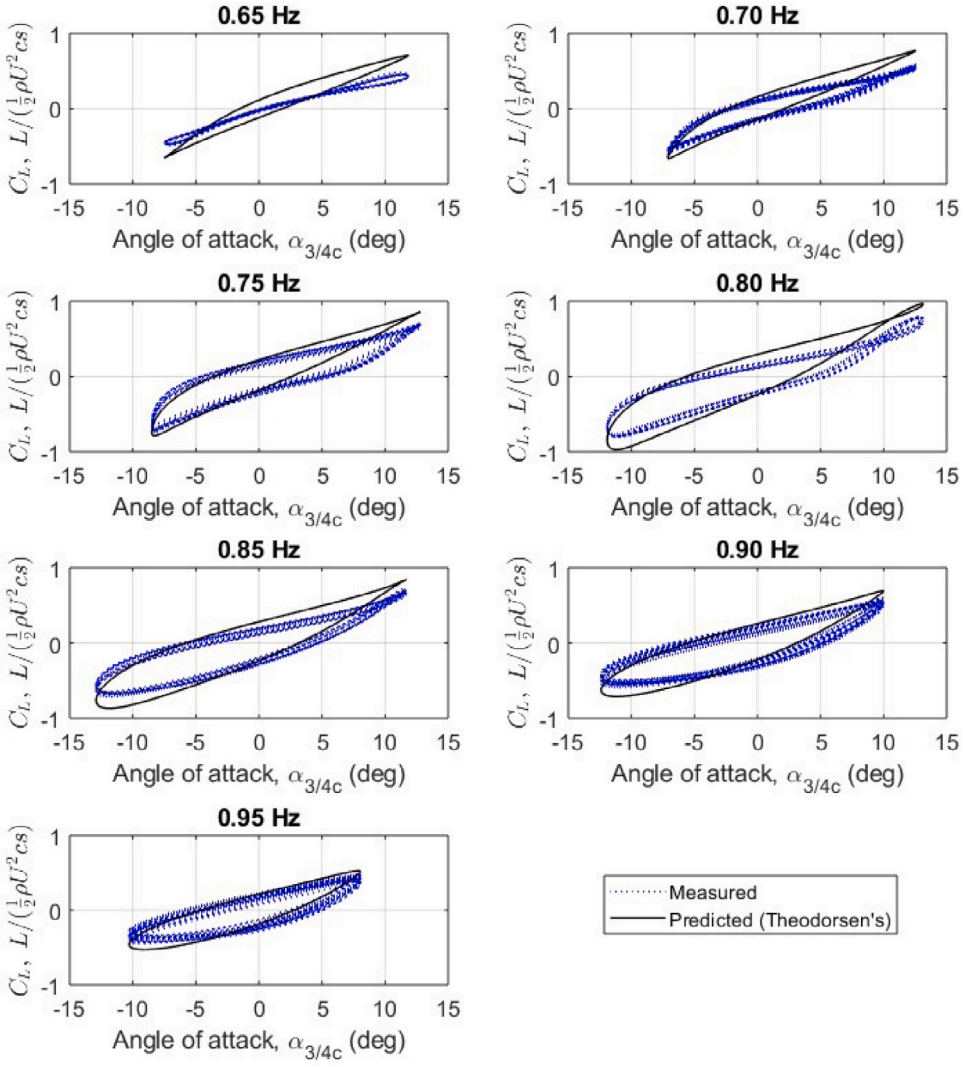

Fig. 19. Measured lift coefficient against the estimated effective angle of attack at the three-quarter chord location, and the theoretical prediction based on Theodorsen's unsteady foil theory.

5. Conclusions

This study demonstrates an improved experimental procedure for free running model tests to evaluate the effect of bow foils on the engine load of a ship in waves.

The results of the model scale tests show that the bow foil provides a significant reduction in propulsive power required to maintain a constant speed in waves and by association a significant reduction in emissions is achievable. The free running model with a spring-loaded foil system, demonstrated an average ship pitch and heave reduction of 20% and 10% respectively, and a reduction of delivered power of up to 50% in regular head waves, and an estimated reduction of 12% in irregular head waves with directional spreading.

The experimental results show that the flapping phase and feathering parameter could prove to be useful metrics for bow foil optimisation with respect to the relative contributions of foil thrust and reduced ship motions.

CRediT authorship contribution statement

J.A. Bowker: Methodology, Validation, Formal analysis, Investigation, Data curation, Writing – original draft, Visualisation. **N.C. Townsend:** Conceptualisation, Methodology, Software, Investigation, Writing – review & editing, Supervision, Funding acquisition.

Declaration of competing interest

The authors declare that they have no known competing financial interests or personal relationships that could have appeared to influence the work reported in this paper.

Acknowledgements

The authors would like to thank Mathew Lamont for the development of the ship database and initial hullform design during his summer internship.

This research was supported by the EU as part of the SeaTech project (https://seatech2020.eu/). All authors approved the final version of the manuscript.

This project has received funding from the European Union's Horizon 2020 research and innovation programme under grant agreement No 857840

The opinions expressed in this document reflect only the author's view and in no way reflect the European Commission's opinions. The European Commission is not responsible for any use that may be made of the information it contains.

References

Abbott, I., Von Doenhoff, A., 1959. Theory of Wing Sections: Including a Summary of Airfoil Data. Dover Publications.

Abkowitz, M.A., 1959. The Effect of Antipitching Fins on Ship Motions, Vol. 67. The Society of Naval Architects and Marine Engineers, SNAME'74, Trinity Place, New York, USA, Paper No. 1, SNAME Transactions 1959.

Anon, 2019. Propulsion trends in bulk carriers. MAN Energy Solutions.

Anon, 2021c. Wavefoil. www.wavefoil.com. (Accessed: 18 August 2021).

Belibassakis, K., Bleuanus, S., Vermeiden, J., Townsend, N., 2021. Combined performance of innovative biomimetic ship propulsion system in waves with dual fuel ship engine and application to short-sea shipping. In: The 31st International Ocean and Polar Engineering Conference. OnePetro.

Belibassakis, K.A., Filippas, E.S., 2015. Ship propulsion in waves by actively controlled flapping foils. Appl. Ocean Res. 52, 1–11. http://dx.doi.org/10.1016/j.apor.2015.04.009, URL https://www.sciencedirect.com/science/article/pii/S0141118715000541.

Belibassakis, K.A., Politis, G.K., 2013. Hydrodynamic performance of flapping wings for augmenting ship propulsion in waves. Ocean Eng. 72, 227–240. http://dx.doi.org/10.1016/j.oceaneng.2013.06.028, URL https://www.sciencedirect.com/science/article/pii/S0029801813002746.

Bockmann, E., 2015. Wave Propulsion of Ships (Ph.D. thesis). NTNU.

Bockmann, E., Steen, S., 2014. Experiments with actively pitch-controlled and spring-loaded oscillating foils. Appl. Ocean Res. 48, 227–235. http://dx.doi.org/10.1016/j.apor.2014.09.004, URL https://www.sciencedirect.com/science/article/pii/S0141118714000923.

Bockmann, E., Steen, S., 2016. Model test and simulation of a ship with wavefoils. Appl. Ocean Res. 57, 8–18. http://dx.doi.org/10.1016/j.apor.2016.02.002, URL https://www.sciencedirect.com/science/article/pii/S0141118716300244.

Bockmann, E., Yrke, A., Steen, S., 2018. Fuel savings for a general cargo ship employing retractable bow foils. Appl. Ocean Res. 76, 1–10. http://dx.doi.org/10.1016/j.apor.2018.03.015, URL https://www.sciencedirect.com/science/article/pii/S0141118717304091.

Bowker, J., 2018. Coupled Dynamics of a Flapping Foil Powered Vessel (Ph.D. thesis). University of Southampton.

Bowker, J.A., Tan, M., Townsend, N.C., 2021. Forward speed prediction of a free-running wave-propelled boat. IEEE J. Ocean. Eng. 46 (2), 402–413. http://dx.doi.org/10.1109/JOE.2020.2990143.

De Silva, L.W.A., Yamaguchi, H., 2012. Numerical study on active wave devouring propulsion. J. Mar. Sci. Technol. 17 (3), 261–275. http://dx.doi.org/10.1007/s00773-012-0169-y.

Dybdahl, K., 1988. Foilpropellen kan revolusjonere skipsfarten. Teknisk Ukeblad/Teknikk 39, 10–11.

Feng, P., Ma, N., Gu, X., 2014. A practical method for predicting the propulsive performance of energy efficient ship with wave devouring hydrofoils at actual seas. Proc. Inst. Mech. Eng. M: J. Eng. Marit. Environ. 228 (4), 348–361. http://dx.doi.org/10.1177/1475090213489674, URL https://journals.sagepub.com/doi/abs/10.1177/1475090213489674.

Filippas, E.S., 2015. Augmenting ship propulsion in waves using flapping foils initially designed for roll stabilization. Procedia Comput. Sci. 66, 103–111. http://dx.doi.org/10.1016/j.procs.2015.11.013, URL https://www.sciencedirect.com/science/article/pii/S1877050915033621.

Filippas, E., Belibassakis, K., 2014. Hydrodynamic analysis of flapping-foil thrusters operating beneath the free surface and in waves. Eng. Anal. Bound. Elem. 41, 47–59. http://dx.doi.org/10.1016/j.enganabound.2014.01.008, URL https://www.sciencedirect.com/science/article/pii/S0955799714000101.

Filippas, E.S., Papadakis, G.P., Belibassakis, K.A., 2020. Free-surface effects on the performance of flapping-foil thruster for augmenting ship propulsion in waves. J. Mar. Sci. Eng. 8 (5), URL https://www.mdpi.com/2077-1312/8/5/357.

Gawn, R., 1953. Effect of pitch and blade width on propeller performance. In: Autumn Meeting of the Institution of Naval Architects, TINA, Rome, Italy, 1953, 157–193, RINA Transactions 1953-09.

Grue, J., Mo, A., Palm, E., 1988. Propulsion of a foil moving in water waves. J. Fluid Mech. 186, 393–417. http://dx.doi.org/10.1017/S0022112088000205, URL https://www.cambridge.org/core/article/propulsion-of-a-foil-moving-in-water-waves/DF02E53C625251EE98EC47CD06AF767D.

Huang, S., Wu, T., Hsu, Y., Guo, J., Tsai, J., Chiu, F., 2016. Effective energy-saving device of eco-ship by using wave propulsion. In: 2016 Techno-Ocean. Techno-Ocean, pp. 566–570. http://dx.doi.org/10.1109/Techno-Ocean.2016.7890719.

IMO, 2011. Amendments to the annex of the protocol of 1997 to amend the international convention for the provention of pollution from ships, 1973, as modified by the protocal of 1978 relatiing thereto. (Resolution MEPC.203(62)). International Maritime Organisation (IMO).

IMO, 2018. International Code on Intact Stability, third ed. International Maritime Organisation (IMO).

Isshiki, H., 2015. Improvement of ship performance under rough weather by utilizing wave energy. Asian J. Eng. Technol. 03, 329–333. http://dx.doi.org/10.14856/conf.22.0_329.

Isshiki, H., Murakami, M., 1984. A theory of wave devouring propulsion (4th Report); A comparison between theory and experiment in case of a passive-type hydrofoil propulsor. J. Soc. Nav. Archit. Jpn 156, 102–114.

ITTC, 1957. ITTC model-ship correlation line. In: 8th International Towing Tank Conference. ITTC.

ITTC, 2008. Guide to the Expression of Uncertainty in Experimental Hydrodynamics. 7.5-02-01-01, Recommend Procedures and Guidelines, ITTC.

ITTC, 2011. Final Report and Recommendations to the 26th ITTC. The Resistance Committee, ITTC.

ITTC, 2017a. Seakeeping Experiments. 7.5-02-07-02.1, Seakeeping Committee of the 29th ITTC.

ITTC, 2017b. 1978 ITTC Performance Prediction Method. 7.5-02-03-01.4, Propulsion Committee of the 28th ITTC 2017.

ITTC, 2021a. Final Report and Recommendations to the 29th ITTC. The Special Committee on Energy Saving Methods, ITTC.

ITTC, 2021b. Prediction of Power Increase in Irregular Waves from Model Tests. 7.5-02-07-02.2, Seakeeping Committee of the 29th ITTC.

Jakobsen, E., 1981. The foil propeller, wave power for propulsion. In: 2nd International Symposium on Wave and Tidal Energy, Vol. 1981. pp. 363–369, URL https://ci.nii.ac.jp/naid/80001169029/en/.

Jones, R., 1940. The Unsteady Lift of a Wing of Finite Aspect Ratio. Tech. Rep. Report No. 629, NACA.

Linden, H., Improved combination with floating bodies, of fins adapted to effect their propulsion, GB Patent, 14, 1895.

Liu, J., Hekkenberg, R., 2017. Sixty years of research on ship rudders: effects of design choices on rudder performance. Ships Offshore Struct. 12 (4), 495–512.

Miley, S.J., 1982. A Catalog of Low Reynolds Number Airfoil Data for Wind Turbine Applications. Tech. Rep. RFP-3387, Texas A&M University of Rockwell International Corporation.

Molland, A., Turnock, S., Hudson, D., 2017. Ship Resistance and Propulsion, second ed. Cambridge University Press.

Naito, S., Isshiki, H., 2005. Effect of bow wings on ship propulsion and motions. Appl. Mech. Rev. 58 (4), 253–268. http://dx.doi.org/10.1115/1.1982801.

Naito, S., Isshiki, H., Fujimoto, K., 1986. Thrust generation of a fin attached to a ship in waves. J. Kansai Soc. Nav. Archit..

Nikolaev M.N., A., Senkin, Y., 1995. Basics of calculation of the effciency of a ship with propulsor of the wing type. Sudostroenie 4, 7–10.

Ol, M.V., Bernal, L., Kang, C., Shyy, W., 2009. Shallow and deep dynamic stall for flapping low Reynolds number airfoils. Exp. Fluids 46, 883–901.

Pistolesi, E., 1933. Considerazioni sul problema delbiplano. Aerotecnica.

Robinson, A., 2008. Guide to the Calibration and Testing of Torque Transducers. Tech. Rep. 107, National Physics Laboratory.

Rozhdestvensky, K.V., Htet, Z.M., 2021. A mathematical model of a ship with wings propelled by waves. J. Mar. Sci. Appl..

Seo, J.-H., Lee, C.-M., Yu, J.-W., Choi, J.-E., Lee, I., 2020. Power increase and propulsive characteristics in regular head waves of KVLCC2 using model tests. Ocean Eng. 216, 108058. http://dx.doi.org/10.1016/j.oceaneng.2020.108058, URL https://www.sciencedirect.com/science/article/pii/S0029801820310003.

Stefun, G.P., 1959. Model experiments with fixed bow antipitching fins. J. Ship Res. 3 (03), 14–23. http://dx.doi.org/10.5957/jsr.1959.3.3.14.

Terao, Y., Isshiki, H., 1991. Wave devouring propulsion sea trial. In: Eighteenth Symposium on Naval Hydrodynamics. pp. 297–296.

Theodoersen, T., 1935. General Theory of Aerodynamic Instability and the Mechanism of Flutter. Tech. Rep. Report No. 496, NACA.

Triantafyllou, G.S., Gopalkrishnan, R., 1991. Wake mechanics for thrust generation in oscillating foils. Phys. Fluids A 3 (12), 2835–2837.

Ueno, M., Tsukada, Y., 2016. Estimation of full-scale propeller torque and thrust using free-running model ship in waves. Ocean Eng. 120, 30–39. http://dx.doi.org/10.1016/j.oceaneng.2016.05.005, URL https://www.sciencedirect.com/science/article/pii/S0029801816301160.

Wu, T., 1972. Extraction of flow energy by a wing oscillating in waves. J. Ship Res. 16 (01), 66–78. http://dx.doi.org/10.5957/jsr.1972.16.1.66.

Wu, T.N., Guo, J., Chen, Y.N., Chen, W.C., 1996. Experimental study of ship pitching motion reduction using anti-pitching fins. In: Proceedings of the JFPS International Symposium on Fluid Power, vol. 1996, no. 3. pp. 223–228. http://dx.doi.org/10.5739/isfp.1996.223.